RSC Advances

PAPER

View Article Online
View Journal | View Issue



Cite this: *RSC Adv.*, 2026, **16**, 28751

# Biosynthesis of copper, cobalt, and zinc oxide nanoparticles using the seed extract of *Citrullus lanatus* and determination of biological potentials

Wajeeha Gohar,[a] Khalil Nawaz,[a] Wardha Zafar,[a] Ambreen Nasir Cheema,[b] Nadeem Raza,[c] Muddassar Zafar,[d] Muhammad Faizan Nazar[e] and Sajjad Hussain Sumrra *[a]

The research is based on using a greener approach for synthesizing cobalt oxide, copper oxide, and zinc oxide nanoparticles using the seed extract of *Citrullus lanatus* (CL). The synthesized nanoparticles were characterized by UV-vis, FT-IR spectroscopy, XRD, SEM, and EDX analysis. Scanning electron microscopy (SEM) analysis revealed that the particles are uniformly distributed with average sizes of 146.49 ± 45.15, 176.37 ± 50.47, and 123.61 ± 27.26 nm for $Co_3O_4$, CuO, and ZnO nanoparticles, respectively. The crystalline nature of the nanoparticles was confirmed by X-ray diffraction (XRD), which revealed average particle sizes of 12.38, 10.46, and 11.76 nm for $Co_3O_4$, CuO, and ZnO nanoparticles, respectively. The specific surface area (SSA) was calculated to be 79.84, 90.90, and 90.94 $m^2\ g^{-1}$ for $Co_3O_4$, CuO, and ZnO, respectively. A maximum inhibition diameter of 15 mm was exhibited by CuO and ZnO against *S. aureus* and *B. subtilis*. ZnO nanoparticles exhibited 90% and 81% activity in the DPPH and total phenolic content assays, respectively. Maximum α-amylase and protease inhibition activities were demonstrated by the $Co_3O_4$ and ZnO nanoparticles, with values of about 62% and 71%, respectively.

Received 9th March 2026
Accepted 1st May 2026

DOI: 10.1039/d6ra02015a

rsc.li/rsc-advances



## 1. Introduction

In the recent decades, nanoparticles have attracted increasing attention as they bridge the gap between bulk materials and atomic-level structures. Their large surface-area-to-volume ratio leads to pronounced alterations in their physical, chemical, and biological properties relative to bulk materials, resulting in enhanced reactivity, improved functional performance, and expanded application potential across multiple scientific and technological domains.[1] The chemical properties of the nanoparticles have been used in anti-bacterial, anti-fungal, anti-corrosive, antioxidant, and environmental applications.[2] Green synthesis has emerged as a widely explored approach for synthesizing different metal and metal oxide-based nanoparticles. It is an environmentally benign and economically feasible method that leads to the formation and development of stable, sustainable, biocompatible nanoparticles in a short period using molecules extracted from various parts of plants.[3] The green synthesis of nanoparticles is straightforward, comprising low-cost, environment-friendly, and non-toxic reagents,[4] and metal-based nanoparticles can be synthesized on a large scale using this simple method. The extracts produced from plants act as natural bio-reductants and capping agents that increase the stability of the nanoparticles.[5] All these qualities have attracted the attention of researchers. The method involves the bio-reduction of metal ions along with the subsequent growth and stabilization of nanoparticles.[6]

The distinctive and unique physical and chemical properties of nanomaterials can be used for applications that benefit society. In the field of medicinal science, they have been used in tissue engineering,[7] drug delivery,[8] gene therapy,[9] in the treatment of wounds,[10] and as antimicrobial agents.[11] In the textile industry, stain- and wrinkle-resistant clothes are examples of innovations based on these nanoparticles.[12] Flexible materials, anti-corrosive paints, and lightweight armours have been made possible because of nanoparticles. Furthermore, nanoparticles find applications in glucose sensors,[13] solar panels,[14] and lithium-ion batteries.[15] Hence, nanoparticles are used in everyday life, improving convenience and accessibility. Nanoparticles synthesized *via* green routes have potent applications in medicine as targeted drug-delivery agents and are used as antimicrobial agents.[16,17] They also have antioxidant properties.[18,19] Copper nanoparticles that are biologically synthesized have good potential against plant pathogens. The growth of

[a]*Department of Chemistry, University of Gujrat, Gujrat 50700, Pakistan. E-mail: sajjadchemist@gmail.com; sajjadchemist@uog.edu.pk*

[b]*Department of Chemistry, University of Engineering and Technology, Lahore 54890, Pakistan*

[c]*Department of Chemistry, College of Science, Imam Mohammad Ibn Saud Islamic University, Riyadh, Saudi Arabia*

[d]*Department of Biochemistry and Biotechnology, University of Gujrat, Gujrat 50700, Pakistan*

[e]*Department of Chemistry, Division of Science and Technology, University of Education, Multan Campus, Lahore, Pakistan*

plant-infecting bacteria, *i.e.*, *Lolium perenne*, *Raphanus sativus*, and *Lolium rigidum*, is inhibited by copper nanoparticles.[20] ZnO nanoparticles are used in sunscreen as they tend to block UV rays. These nanoparticles also find applications as anti-aging agents because they are powerful antioxidants that meet the safety requirement of not penetrating deep into the skin; moreover, they are not carcinogenic or cytotoxic.[21]

The antiviral potential of ZnO and $SiO_2$ nanoparticles was assessed against the tobacco mosaic virus.[22] Copper nanoparticles that are biologically synthesized have good potential against plant pathogens. The bio-assisted synthesis of cobalt oxide nanoparticles was achieved utilizing the herbal extract of *P. dactylifera*. The synthesized nanoparticles were proven to be potent antibacterial and antifungal agents and are efficient for the degradation of dyes.[23] *Cynodon dactylon* was used to synthesize copper nanoparticles. The synthesized nanoparticles were evaluated by their biological activities and their potential for dye degradation.[24] The green essence of sea lavender leaves was used as a reducing, stabilizing, and capping agent, and the anti-cancer activity assessments for epidermal cells showed that cell viability decreased significantly.[25] Anthony Ekennia and coworkers used the aqueous extracts of *Alchornea laxiflora* leaves along with the respective salt of zinc to synthesize zinc oxide nanoparticles. The nanoparticles exhibited moderate photocatalytic potency, with 87% degradation of Congo red dye.[26] *Nigella sativa* seed extracts were used to synthesize copper nanoparticles. The particle size of nanoparticles was 98.23 nm, and they exhibited potent antibacterial action, with 25 mm and 24 mm inhibition zones against *E. coli* and *P. aeruginosa*, respectively. Lipase and amylase inhibition assays also confirmed their antiobesity activities.[27] Leaf extracts of *Moringa olifera* and *Musa* sp. were used as bio-reducing agents to synthesize Cu and CuO nanoparticles. XRD analysis revealed the cubic phase of CuNPs and the monoclinic phase of CuO. They exhibited potent antibacterial and antioxidant activity.[28]

Synthesizing copper, cobalt, and zinc nanoparticles using *Citrullus lanatus* (watermelon) is a new approach to the formation of nanoparticles. The use of these seed extracts, which are rich in bioactive compounds, imparts specific characteristics to the nanoparticles, including antibiotic, antioxidant, and anti-inflammatory properties. Watermelon seeds have been used against hypertension, gonorrhea, and diarrhea as they contain lycopene, vitamin C, riboflavin, thiamine, polyphenols, terpenes, and steroids.[29] The seeds also contain vanillin, quercetin, kaempferol, luteolin, and myricetin. Palmitic, linoleic, ferulic, chlorogenic, protocatechuic, and *p*-coumaric acids are the main phytochemical acids present, along with other alkaloids, flavonoids, steroids, and terpenoids.[30] These phytochemicals act as stabilizing and reducing agents when treated with respective metal precursors.[31] These nanoparticles have great antibacterial and antioxidant capabilities.

A comprehensive characterization of nanoparticles was performed utilizing X-ray diffraction (XRD) analysis, scanning electron microscopy (SEM), ultraviolet-visible spectroscopy (UV-vis), and Fourier-transform infrared (FT-IR) spectroscopy. These analysis techniques were used for structural elucidation and chemical characterization. The nanoparticles were characterized by UV-visible spectroscopy to study the plasmon bands. The strength and stability of the resonances were determined by the shape, size, and environment, as well as by the dielectric function of the nanoparticles.[32] FT-IR spectroscopy was used to verify the presence of various functional groups attached to the nanoparticles. The crystallinity of the nanoparticles was determined by XRD analysis, and the presence of intrinsic strain, which arises because of size confinement, was confirmed by measuring peak broadening.[33] SEM analysis was used to discover the shape, surface texture and particle size distribution of the nanoparticles.

*Citrullus lanatus* (CL) has attracted attention as a bio-reducing agent due to its rich phytochemical composition. Previous studies have reported the synthesis of ZnO and CuO using CL seed extract, demonstrating promising properties.[34,35] However, no comparative synthesis of multiple metal oxide nanoparticles using a CL seed extract under identical conditions has been reported. Therefore, a systematic comparison of multiple metal oxide nanoparticles synthesized using the same reducing agent under the same conditions remains largely unexplored. Different metal ions exhibit distinct redox behavior, coordination chemistry, and oxide formation pathways; therefore, their interaction with a single biological extract is expected to yield nanoparticles with varied physicochemical characteristics and biological activities. Accordingly, the present study focuses on the synthesis of $Co_3O_4$, CuO, and ZnO nanoparticles using *C. lanatus* seed extract under identical conditions and compares the antioxidant and enzyme-inhibitory activities of the synthesized nanoparticles using multiple complementary assays under controlled conditions. The study offers deeper insights into the structure–activity relationships of the different metal oxides.

In this work, the seed extract of *Citrullus lanatus* (watermelon) served as the reducing agent in the synthesis of cobalt oxide, copper oxide, and zinc oxide nanoparticles. The extract was treated with the metal salt of the respective metals to synthesize the nanoparticles. The nanoparticles were characterized using UV-vis and FT-IR spectroscopy, along with XRD, SEM, and EDX techniques. The research aims to compare the antibacterial, antioxidant, and enzyme-inhibition potential of the synthesized nanoparticles.

## 2. Materials and methods

All the chemicals used in the present work were of analytical grade and purchased from Sigma-Aldrich, USA. Zinc acetate dihydrate, copper sulfate pentahydrate, cobalt nitrate hexahydrate, sodium hydroxide (NaOH), distilled ethanol ($C_2H_5OH$), acetone ($C_3H_6O$), and double-distilled water were used. *Citrullus lanatus* (watermelon) seeds were procured from a local market in Gujrat, Pakistan. The nanoparticles were characterized by UV-vis, FT-IR spectroscopy, SEM, EDX, and XRD analysis. The UV-vis optical spectra were recorded with a Shimadzu UV-1700 spectrophotometer in the range of 200–800 nm. FT-IR spectra of the nanoparticles were recorded with a Nicolet IS-50 FT-IR spectrometer equipped with an attenuated total reflectance (ATR) accessory; the spectra were recorded over a wavenumber range of 400–

 

4000 $cm^{-1}$. The morphology was determined using SEM with a voltage of 20 kV at resolutions of 20.0, 50.0, and 100.0 k×. Using an INCA Energy 250 microanalysis system (EDS) and a Carl Zeiss MA15/EVO 18 scanning electron microscope, morphological and elemental composition analyses were carried out. To determine the elemental composition, EDS was used. The crystal structure and size were analyzed using an XRD diffractometer from 10° to 100° ($2\theta$); Cu-K$\alpha$ radiation was used to obtain the XRD patterns. Antibacterial assays were performed against both Gram-negative (*Escherichia coli* ATCC 10536 and *Pseudomonas aeruginosa* ATCC 10145) and Gram-positive (*Bacillus subtilis* ATCC 6633 and *Staphylococcus aureus* ATCC 25923) bacteria.

### 2.1. Extraction process

The seeds of *Citrullus lanatus* (CL) were chosen because they contain phytochemicals that allow the reduction and eventual stabilization of the synthesized nanoparticles. The seeds were bought from a local market. Dirt and stones were removed, and seeds were washed with distilled water, sun-dried, and ground to a well-powdered form. Thirty grams of dried seeds were used to obtain an extract in a hydroalcoholic solution containing ethanol and water (50 : 50 v/v). The reaction mixture was continuously stirred using a magnetic stirrer at 80 °C for one hour. The Whatman filter paper was used to filter the extract. The procedure was repeated thrice to obtain a better extract so that most of the phytochemicals were extracted in the solvent, and the nanoparticles were reduced with higher efficiency. The CL seed extract obtained was stored at 4 °C in a refrigerator for further use.[36]

### 2.2. Synthesis of the nanoparticles

Metallic oxide nanoparticles were synthesized utilizing metal salt precursors, *i.e.*, zinc acetate dihydrate, copper sulfate pentahydrate, and cobalt nitrate hexahydrate. A salt solution of 0.5 M was prepared in 50 mL of distilled water. The extract was taken in a burette, and about 15 mL of CL seed extract was added dropwise to the metal salt solution under uninterrupted magnetic stirring at 600 rpm for 1 hour, with the temperature maintained at 80 °C. After the addition, 1 M NaOH was added until the pH increased to 12. The reaction was allowed to proceed under continuous stirring for 3 hours. A visible color change in the reaction mixture indicated the formation of nanoparticles. After completion of the reaction, the mixture was left undisturbed for 24 hours at ambient temperature to ensure complete reduction and stabilization of the nanoparticles. The mixture was centrifuged at 10 000 rpm for 30 min at 4 °C to collect the nanoparticles. The nanoparticles were then washed thrice to neutralize the pH, followed by washing with ethanol to remove unreacted compounds. The nanoparticles were then dried in an oven at 120 °C, and the dried nanoparticles were calcinated at 300 °C for 2 hours.[27] A schematic of the synthesis of the nanoparticles is given in Fig. 1.

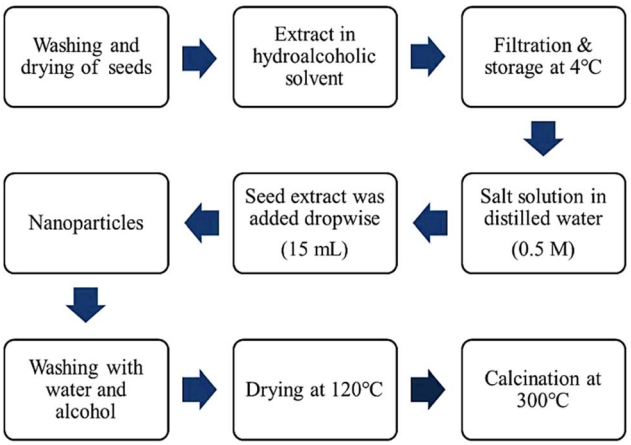


Fig. 1 Schematic of the synthesis of the nanoparticles.

### 2.3. Characterization

**2.3.1. UV-vis spectroscopy.** The UV-vis absorption spectra of $Co_3O_4$, CuO, and ZnO nanoparticles were investigated to evaluate their optical characteristics and band gaps. For the estimation of the band gap, the Wood and Tauc relation was used.[37]

$$\alpha h\nu = B\left(h\nu - E_g\right)^{\frac{1}{n}} \quad (1)$$

where $n$ is the type of transition, $E_g$ is the band gap, $\alpha$ is the absorption coefficient, $h$ is Planck's constant, $\nu$ is the photon frequency, and $B$ is a proportionality constant (which is known as the absorption constant and depends on the transition).

**2.3.2. FT-IR analysis.** The M–O bond force constant ($k$) and bond lengths ($r$) were calculated using the reported method.[38,39] Using vibrational frequencies ($\nu$) of Co–O, Cu–O, and Zn–O bonds, the bond force constant was calculated using eqn (2).

$$k = \mu(2\pi\nu)^2 \quad (2)$$

where $\mu$ represents the reduced mass of the M–O pair determined using eqn (3)

$$\mu = \frac{M_m M_o}{M_m + M_o} \quad (3)$$

where $M_m$ and $M_o$ are the atomic masses of the metals and oxygen, respectively. The M–O bond length is then calculated using the empirical relation given in eqn (4), where $d$ is the constant for the M–O bond.

$$r = \sqrt[3]{\frac{17}{k}} + d \quad (4)$$

**2.3.3. XRD analysis of the nanoparticles.** The diffraction patterns were examined to determine the crystal structure and to calculate the crystallite size using Debye–Scherrer's formula (eqn (5)).[38]

$$D = \frac{k\lambda}{\beta \cos\theta} \quad (5)$$

where $D$ represents the crystallite size, $k$ is the shape factor (commonly taken as 0.9), $\lambda$ corresponds to the X-ray wavelength (1.5406 Å for Cu K$\alpha$ radiation), $\beta$ is the full width at half

maximum (FWHM) of the diffraction peak, and $\theta$ denotes the Bragg angle. In addition, the specific surface area was computed using the crystallite size derived from XRD data with the following relationship (eqn (6)):

$$\mathrm{SSA} = \frac{6 \times 10^3}{D_\mathrm{P} \times \rho} \quad (6)$$

where SSA is the specific surface area, $D_\mathrm{P}$ is the size of the particles, and $\rho$ is the density.

### 2.4. Biological activities

The different biological potentials of the synthesized nanoparticles were evaluated, and the antimicrobial, antioxidant, and enzyme inhibition activities were explored.

**2.4.1. Antibacterial activity of the nanoparticles.** Antimicrobial assays of the synthesized metallic oxide nanoparticles were performed using the disk diffusion method.[40,41] The activity was evaluated against both Gram-positive and Gram-negative bacterial types, including *Bacillus subtilis*, *Staphylococcus aureus*, *Escherichia coli*, and *Pseudomonas aeruginosa*. For the growth of bacterial cultures, nutrient media were prepared and autoclaved at 121 °C for 3 hours. Bacterial cultures were mixed in the nutrient media separately when the temperature of the nutrient media was no longer harmful to the bacteria. Sample solutions prepared in DMSO (7 mg $mL^{-1}$) were adsorbed on paper disks. As a control group, the CL seed extract was used to account for its inherent activity. Levofloxacin was the standard drug, and DMSO served as the negative control. Petri dishes were covered with their lids, tightly packed, and placed in an incubator for 24 hours at 33 °C. The diameters of the inhibition zones were measured after the completion of the incubation period.

**2.4.2. Antioxidant activity of the nanoparticles.** The antioxidant activity was assessed using three distinct assays. Total phenolic content was determined utilizing the Folin–Ciocalteu reagent method. The DPPH assay and ferric reduction antioxidant potential were also determined.

*2.4.2.1. Total phenolic content.* Total phenolic content was evaluated by following the reported method[42,43] with some modifications. The sample (0.1 mL, 1 mg $mL^{-1}$ in methanol) was added to test tubes, followed by a sodium carbonate (7.5%) solution. Folin–Ciocalteu reagent (10%) was prepared, and 1 mL of this FC reagent was loaded in the test tubes followed by addition of distilled water to make the total volume up to 10 mL. The samples were stored in the dark at room temperature for about 30 minutes. Using a UV-visible spectrometer, the absorbance at 760 nm was noted. CL seed extract served as a control to evaluate its role in the assay. Gallic acid served as the standard, and the same conditions were used. A blank with no sample was used as a control group, and the same procedure was followed. The antioxidant percentage was determined using eqn (7).

$$\%\ \text{Antioxidant activity} = \left(\frac{\text{Blank} - \text{Sample}}{\text{Blank}}\right) \times 100 \quad (7)$$

*2.4.2.2. DPPH radical scavenging activity.* The synthesized metallic oxide nanoparticles were subjected to the DPPH assay. DPPH is a stable violet-colored radical that gives a maximum absorbance at 517 nm. The absorbance at 517 nm is due to the delocalization of free electrons present on the nitrogen, which gives an intense color. When the reduction occurs, by accepting a hydrogen, the 2,2-diphenyl-1-picrylhydrazyl (DPPH$^\bullet$) is converted into 2,2-diphenyl-1-picrylhydrazine (DPPH-H), and the electrons become localized on the nitrogen atom. The violet color disappears; it does not absorb at 517 nm. The reduction in the absorbance indicates the extent of radical scavenging activity.[44,45] The DPPH radical scavenging activity of the nanoparticles, as determined in the reported method[46] with some modifications, was used. In the test tubes, 0.1 mL of the sample solution (1 mg $mL^{-1}$ in methanol) was loaded. By dissolving 4 mg of DPPH in 100 mL of methanol, a 1 μM solution of DPPH was prepared. In each test tube, 4 mL of methanol was introduced along with 0.1 mL of the sample and 1 mL of freshly prepared DPPH. The test solutions were kept in the dark and at room temperature. The same assay was performed for CL seed extracts. As a standard, BHT was used and was treated the same way as the samples. Further, for a control, a blank solution was prepared that did not contain a sample, and the same procedure was followed. To explore the radical scavenging activity, the absorbance was recorded at 517 nm and compared with that of BHT. To determine the DPPH scavenging activity, eqn (7) was used.

*2.4.2.3. Ferric reduction antioxidant potential.* Ferric reduction potential is influenced by the capability of the antioxidants to reduce the $Fe^{3+}$ into $Fe^{2+}$. The change from the yellow color of the ferric complex to the blue color of the ferrous complex acts as a colorimetric indicator. The reducing agents react with the potassium ferricyanide $K_3[Fe^{3+}(CN)_6]$, and after being reduced, it is converted to potassium ferrocyanide $K_4[Fe^{2+}(CN)_6]$, which reacts with $FeCl_3$, and a ferric–ferrous complex is formed that gives the Prussian blue color, which absorbs at 700 nm. The reduction of ferric iron to ferrous iron in the FRAP assay is shown in Fig. S1. The extent of absorbance indicates the iron reduction potential of the sample.[47] To determine the ferric reduction potential, the reported method[48] was used with a few modifications. In test tubes, the sample solutions were prepared at 1 mg $mL^{-1}$ in methanol. 2.5 mL of the sodium phosphate buffer (2 M, pH 6.6) was added to the test samples, followed by the addition of 5.0 mL of ferricyanide solution (1%). The test tubes were incubated at 50 °C for about 30 minutes. Trichloroacetic acid solution (10% w/v) was prepared, and 5 mL of 10% TCA solution was introduced to the test tubes. The samples were kept for 30 minutes, and 1 mL of a freshly prepared solution of ferric chloride (1%) was added to them. The CL seed extract was treated the same way as described above to evaluate its potential. As a standard antioxidant, BHT was used under the same conditions as those used for the samples to measure its ferric reduction potential. A blank control group was also prepared that did not contain a sample, and the same procedure was followed. The FRAP was calculated using eqn (7).

**2.4.3. Enzyme inhibition activity of the nanoparticles.** The inhibition of α-amylase and protease was explored using the nanoparticles as inhibitors.

*2.4.3.1. α-Amylase inhibition activity.* α-Amylase inhibition activity was studied. The mechanism of action is based on the fact that starch acts as a substrate for α-amylase and is converted into maltose. Maltose is treated with the DNSA reagent, which reduces the 3,5-dinitrosalicylic acid and converts it into 3-amino-5-nitrosalicylic acid, as demonstrated in Fig. S2. The oxidized form of DNSA is yellow, and after being reduced, the color changes to yellow–red, with a maximum absorption at 540 nm. Measuring the absorbance thus reveals the extent of enzyme activity.[49] Activity was determined following the reported method[50] with some modifications. Sample solutions of nanoparticles were prepared in DMSO (2 mg $mL^{-1}$), and 500 μL of the sample solution was added to a test tube. A 0.02 M sodium phosphate buffer was prepared, and the pH was adjusted to 6.9. In the buffer solution, α-amylase was added at a concentration of 0.5 mg $mL^{-1}$. The buffer-amylase solution (500 μL) was then added to the sample solutions, and the test tubes were stored at 25 °C for 10 minutes. Afterwards, 0.5 mL of 1% starch solution was added to the samples, and the test tubes were incubated at 25 °C for 10–15 minutes. DNSA reagent was prepared by adding 1 g of dinitrosalicylic acid to 50 mL of distilled water and 17 g of sodium potassium tartrate. The solution's color became yellow, and then orange-yellow when 20 mL of 2 M NaOH was introduced. The volume of the solution was made up to 100 mL by adding distilled water. In the test tubes, 500 μL of the freshly prepared DNSA reagent solution was added. The test tubes were kept in a water bath, maintaining the temperature at 80 °C. The test solutions were diluted with 5 mL of distilled water. As a control group, the CL seed extract was used to evaluate its role in the activity. Acarbose is widely used as a standard reference inhibitor in α-amylase assays and was used as the positive control to validate the assay. A blank solution was prepared as a negative control group, and the same procedure was followed for both the standard and negative control groups. The absorbance was noted at 540 nm, and eqn (8) was used to determine the percentage inhibition.

$$\% \text{ Inhibition} = \left(\frac{\text{Blank} - \text{Sample}}{\text{Blank}}\right) \times 100 \quad (8)$$

*2.4.3.2. Protease inhibition activity.* Protease (trypsin) inhibition activity was determined to evaluate the potential of the nanoparticles. During the inhibition assay, *N*-benzoyl-DL-arginineparanitroanilide hydrochloride (BA*p*NA) was used as the substrate of the enzyme trypsin; the action of trypsin on BA*p*NA produces *p*-nitroaniline, which is spectroscopically determined at its maximum absorbance at 405 nm. Digestion of BA*p*NA by trypsin is shown in Fig. S3. The activity was determined using the reported method[51] with some modifications. In the test tubes, 100 μL of sample (2 mg $mL^{-1}$ of DMSO) and 300 μL of trypsin solution (1 mg $mL^{-1}$) were added. Tris buffer was prepared with a molarity of 100 mM, and the pH was maintained at 7.5. To the test samples, 1 mL of the tris–HCl was added, and the samples were stored at room temperature for 15 minutes. *N*-Benzoyl-DL-arginineparanitroanilide hydrochloride (BA*p*NA) was added to the test tubes as a substrate. The test tubes were incubated at 37 °C for 45 minutes, and the absorbance was recorded at 405 nm. The CL seed extract was used as a control group. Aprotinin, a competitive protease inhibitor, was employed as a positive standard reference inhibitor to validate the assay. A blank solution was prepared as a negative control group, and the same procedure was followed for both the standard and negative control groups. The percentage inhibition for the protease inhibition activity was calculated using eqn (8).

# 3. Results and discussion

## 3.1. UV-visible analysis of nanoparticles

The simplest method by which nanoparticles are characterized is UV-visible spectroscopy. The principle of the characterization is based on the absorption of ultraviolet or visible light by the nanoparticles in the specific regions compared with the intensity of light absorbed by the reference. The $\lambda_{max}$ values for $Co_3O_4$, CuO, and ZnO were 681, 539, and 485 nm, respectively, as represented in Fig. 2. These are associated with the electronic transition characteristics of metal oxides.[52]

The optical band gap of $Co_3O_4$, CuO, and ZnO, calculated using the method described above, is given in Table 1. For the band gap, a graph was plotted using $h\nu$ on the *x*-axis and $(ah\nu)^2$ on the *y*-axis. The band gap was computed by extrapolating the curved line.

## 3.2. FT-IR analysis of nanoparticles

FT-IR analysis was used to characterize the nanoparticles by examining the characteristic peaks of the metal and metal nanoparticles in the spectra. The range of the FT-IR spectra was 4000–400 $cm^{-1}$. The bands in specific regions in the FT-IR spectra are due to different characteristic properties of the nanoparticles.[53] The phytochemicals incorporated in the nanoparticles synthesized by the green method can therefore be studied by FT-IR spectroscopy. The FT-IR spectra of the salt solutions were also obtained and compared with those of the respective metallic oxide nanoparticles, confirming the synthesis of the nanoparticles.

A broad absorption band in the spectrum of the CL seed extract was observed in the region of 3200–3500 $cm^{-1}$, reflecting O–H stretching vibrations, due to phenolic or alcoholic functional groups. An absorption band appeared at 1650–1670 $cm^{-1}$, indicating C=O stretching due to the contribution from the conjugated carbonyl groups present in the flavonoids, phenols, or organic acids. A prominent absorption peak at ~1100 $cm^{-1}$ is due to C–O stretching vibrations, reflecting the presence of alcohols and ethers. For the metal salt precursors, discrete and definite peaks of the respective anions were observed. A strong band was observed in the region of 1050–1130 $cm^{-1}$ corresponding to the asymmetric stretching of $NO_3^{-1}$ in the case of cobalt nitrate.[54] For zinc acetate, asymmetric and symmetric stretching vibrations were observed around 1550–1650 $cm^{-1}$ and 1400–1450 $cm^{-1}$, respectively, due

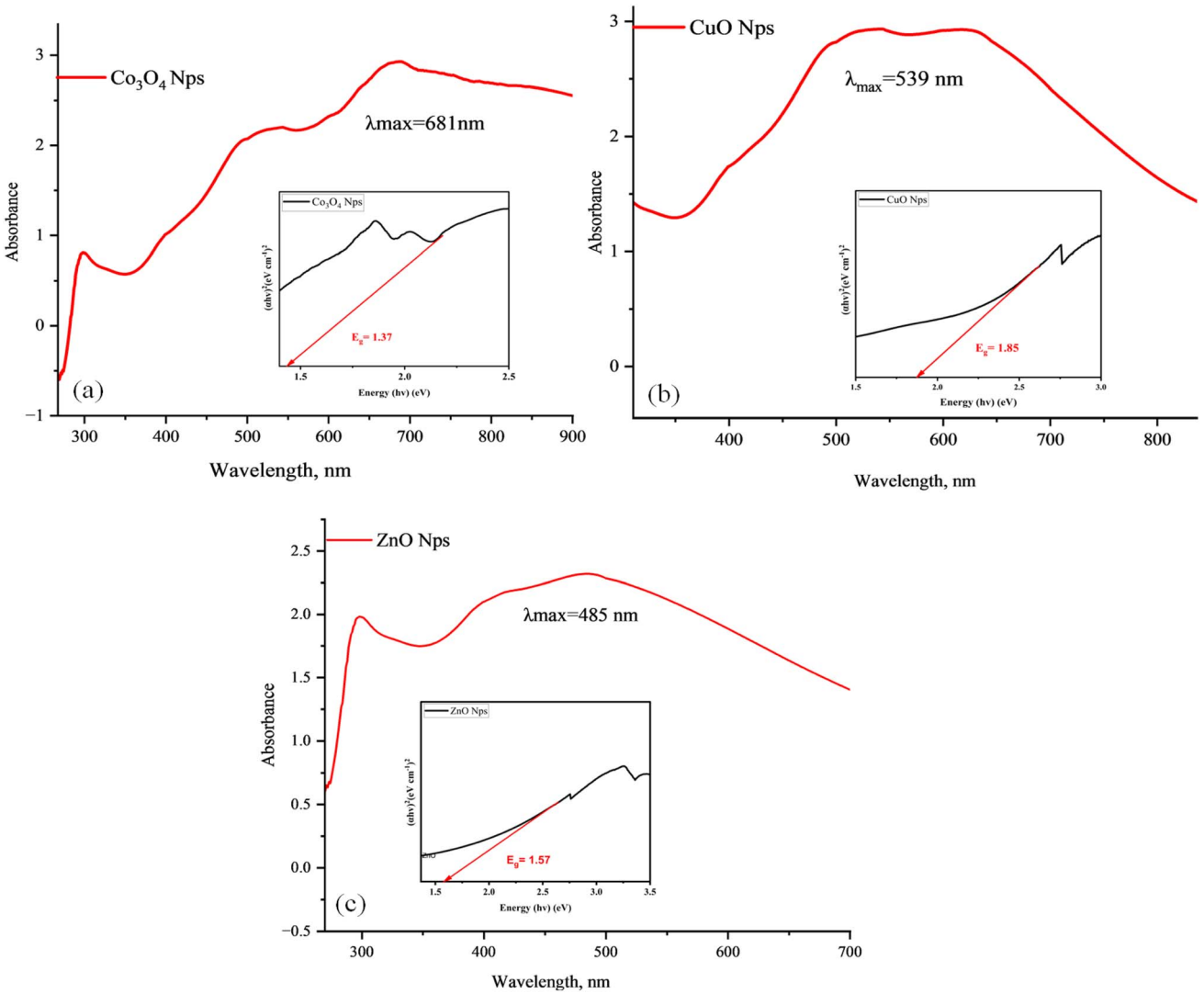


Fig. 2 UV-vis spectra of (a) $Co_3O_4$, (b) CuO, (c) ZnO nanoparticles.

Table 1 $\lambda_{max}$ and band gap energies of $Co_3O_4$, CuO, and ZnO nanoparticles

| S. No. | Metal oxide nanoparticles | $\lambda_{max}$ (nm) | Band gap energy $E_g$ (eV) |
|---|---|---|---|
| 1 | $Co_3O_4$ | 681 | 1.37 |
| 2 | CuO | 539 | 1.85 |
| 3 | ZnO | 485 | 1.57 |

to the presence of $COO^{-1}$.[55] Similarly, a characteristic peak of $SO_4^{2-}$ was present in the region of 1100–1200 $cm^{-1}$ due to S–O stretching vibrations in the case of copper sulphate.[56] The band appearing near 1640–1700 $cm^{-1}$ is primarily attributed to the bending vibrations of H–O–H, which appears in the region due to hydration and moisture absorbed by the metal salts.[57] The $Co_3O_4$ nanoparticles gave two distinct peaks in each spectrum, describing the $Co^{3+}$ and $Co^{4+}$ oxidation state of the nanoparticle and giving the vibrational frequencies of the O–Co–O and Co–O bonds. Peaks of the $Co_3O_4$ nanoparticles were observed at 560 and 660 $cm^{-1}$. The CuO nanoparticles gave peaks in the region of 520–620 $cm^{-1}$, while the stretching vibrational frequency is in the range of 1100–1300 $cm^{-1}$. The synthesized CuO nanoparticles peaks were observed at 601, 883, and 1120 $cm^{-1}$. Peaks in the region of 600–700 $cm^{-1}$ confirm the presence of ZnO, and a peak for the synthesized ZnO was observed at 636 $cm^{-1}$. The presence of these peaks confirmed the formation of these nanoparticles. FTIR analysis exhibited significant structural changes from the seed extract and respective salt to the corresponding nanoparticles, as presented in Fig. 3.

Reduction and shifting of organic functional group peaks suggest their involvement in nanoparticle reduction and stabilization. The M–O bond lengths were calculated and are given in Table 2.

### 3.3. EDX analysis of nanoparticles

To determine the elemental composition of the nanoparticles, EDX spectral analysis was performed. The resulting spectra were in accordance with the results obtained by FT-IR

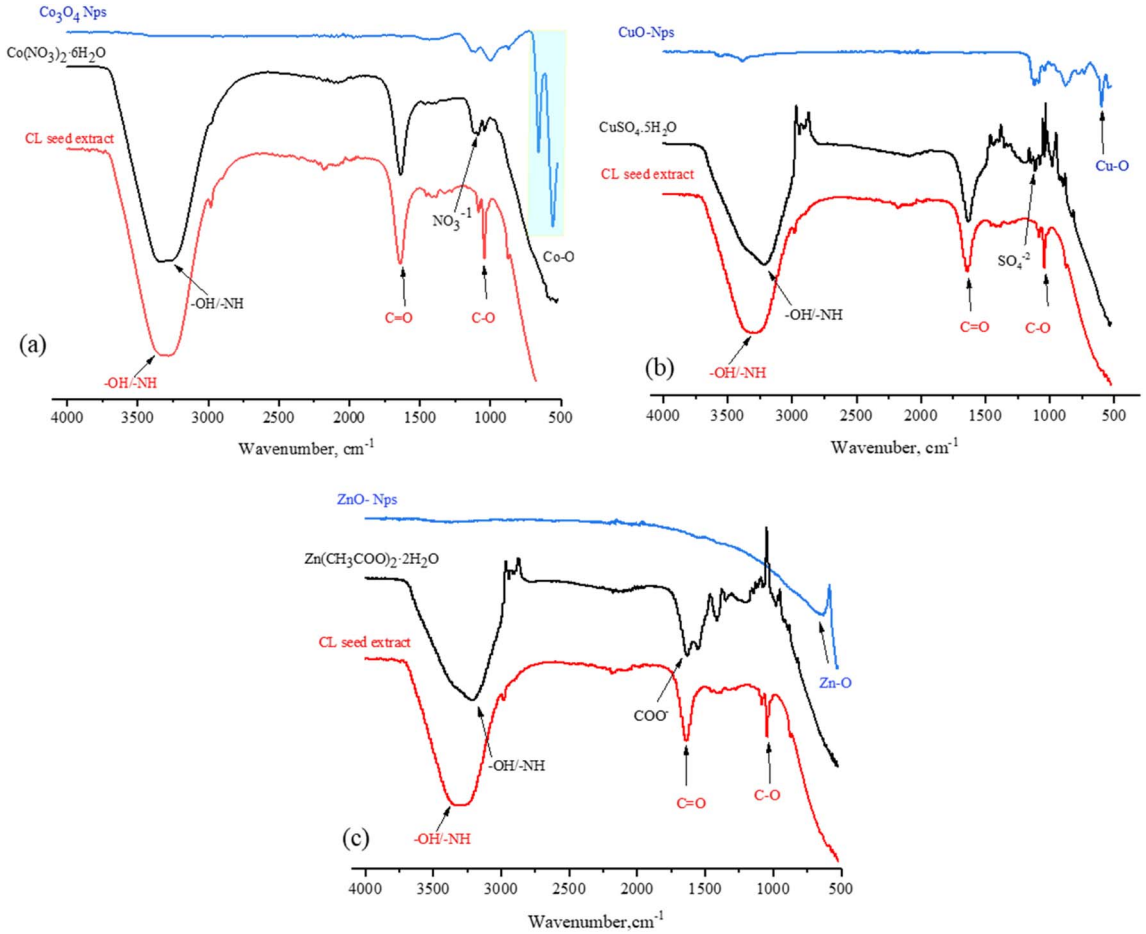


Fig. 3 FT-IR spectra of (a) $Co_3O_4$, (b) CuO, and (c) ZnO nanoparticles.

Table 2 Bond length of the M–O bonds calculated from the wavenumber

| S. No. | Metal–oxygen bond | Wavenumber ($cm^{-1}$) | Bond length (Å) |
|---|---|---|---|
| 1 | O–Co–O | 660 | 1.22 |
| 2 | Co–O | 560 | 1.27 |
| 3 | Cu–O | 600 | 1.25 |
| 4 | Zn–O | 636 | 1.23 |

spectroscopy and XRD, as given in Fig. 4. The EDX spectrum for the $Co_3O_4$ nanoparticles exhibited sharp cobalt peaks. The EDS spot for analysis is shown in Fig. S4, and complete spectral details are given in Table S1. The EDX spectral analysis showed that cobalt was present in 83.47 weight percentage (wt%)and 63.50 atomic percentage (at%), while oxygen was present in 9.03 wt% and 25.40 at%; silica and calcium peaks were also present, which may be due to phytochemicals from the seed extracts that acted as stabilizing and capping agents. The EDS spot for the characterization of copper nanoparticles is shown in Fig. S5, and details are given in Table S2. The CuO nanoparticles confirmed the presence of copper (87.73 wt% and 74.20 at%) and oxygen (2.09 wt% and 7.01 at%). Further, sulphur peaks were also present (4.72 wt% and 7.91 at%), which might be due to phytochemicals or the salt precursor used for the synthesis of the nanoparticles. In the EDX spectrum of ZnO, it was evident that zinc and oxygen were present with high purity. To characterize zinc oxide nanoparticles, an EDS spot was taken, as shown in Fig. S6; the details are given in Table S3. Zinc was present in 99.48 wt% and 97.90 at%, while oxygen was present in 0.52 wt% and 2.10 at%. No additional peak was present in the spectrum, indicating the purity of the ZnO nanoparticles. Notably, EDX analysis showed a slight deviation from the stoichiometric ratios of $CO_3O_4$, CuO, and ZnO nanoparticles, which may be due to incomplete removal of biomolecules from the plant extract. It is important to add that EDX is a semi-quantitative technique that may not provide exact stoichiometric ratios for lighter elements such as oxygen. Moreover, surface-bound biomolecules and nanoparticle agglomeration may influence the measured elemental ratio. Nevertheless, the dominant peaks of Co, Cu, and Zn confirmed the successful synthesis of the respective M–O nanoparticle.

### 3.4. SEM analysis of nanoparticles

SEM images of the nanoparticles are shown in Fig. 5. The SEM images of cobalt oxide reveal the rough, flaky surface with spaces between the flakes, which suggests a porous surface with increased surface area. SEM images of the $Co_3O_4$ nanoparticles

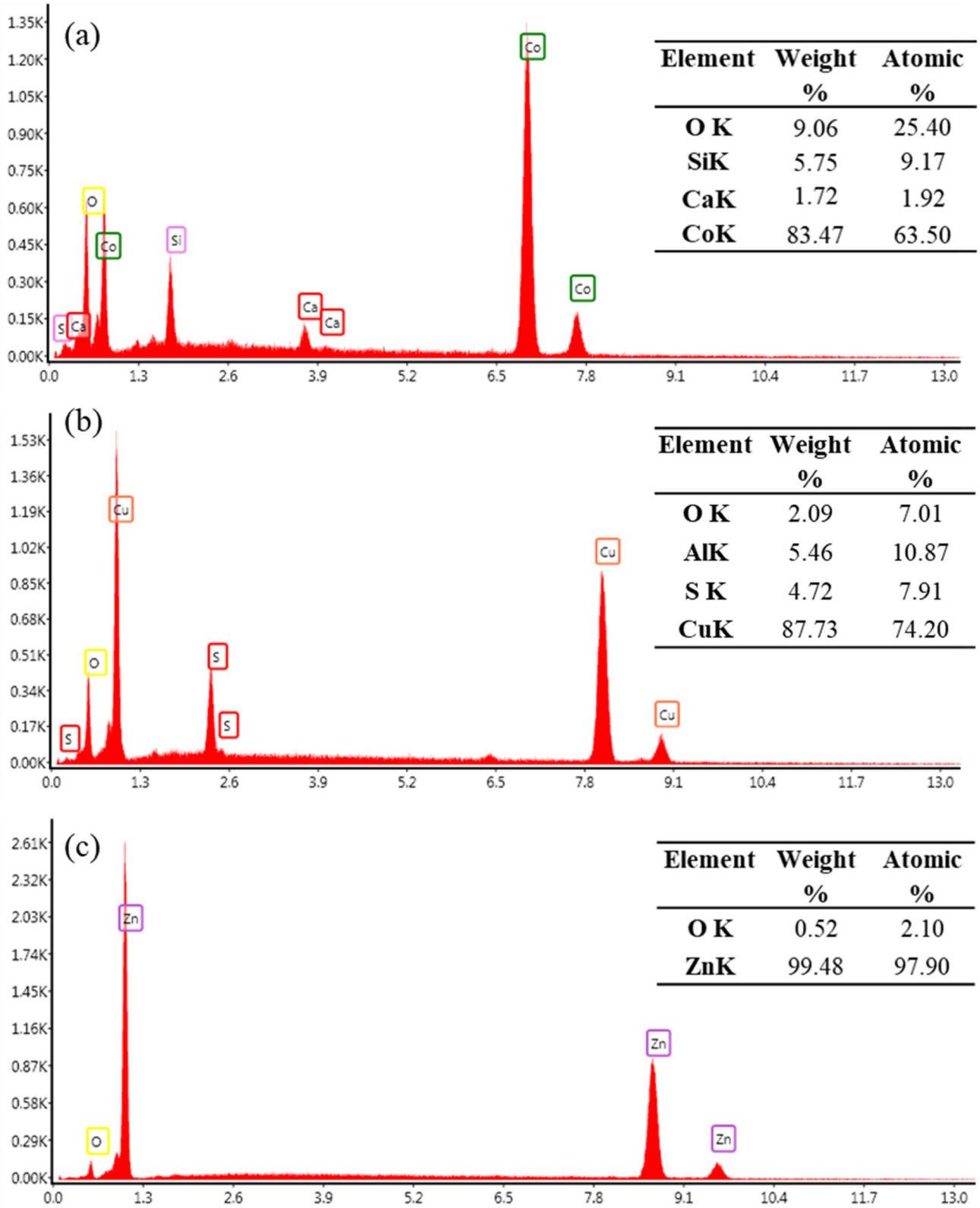


Fig. 4 EDX spectra of (a) $CO_3O_4$, (b) CuO, and (c) ZnO nanoparticles.

were taken at resolutions of 2 μm, 1 μm, and 500 nm. The image at higher resolution depicts layered flakes, which may be due to agglomeration of the nanoparticles.

The SEM image of the CuO nanoparticles revealed the spherical structure of the nanoparticles, with smooth topographic characteristics. It was found that they have smooth

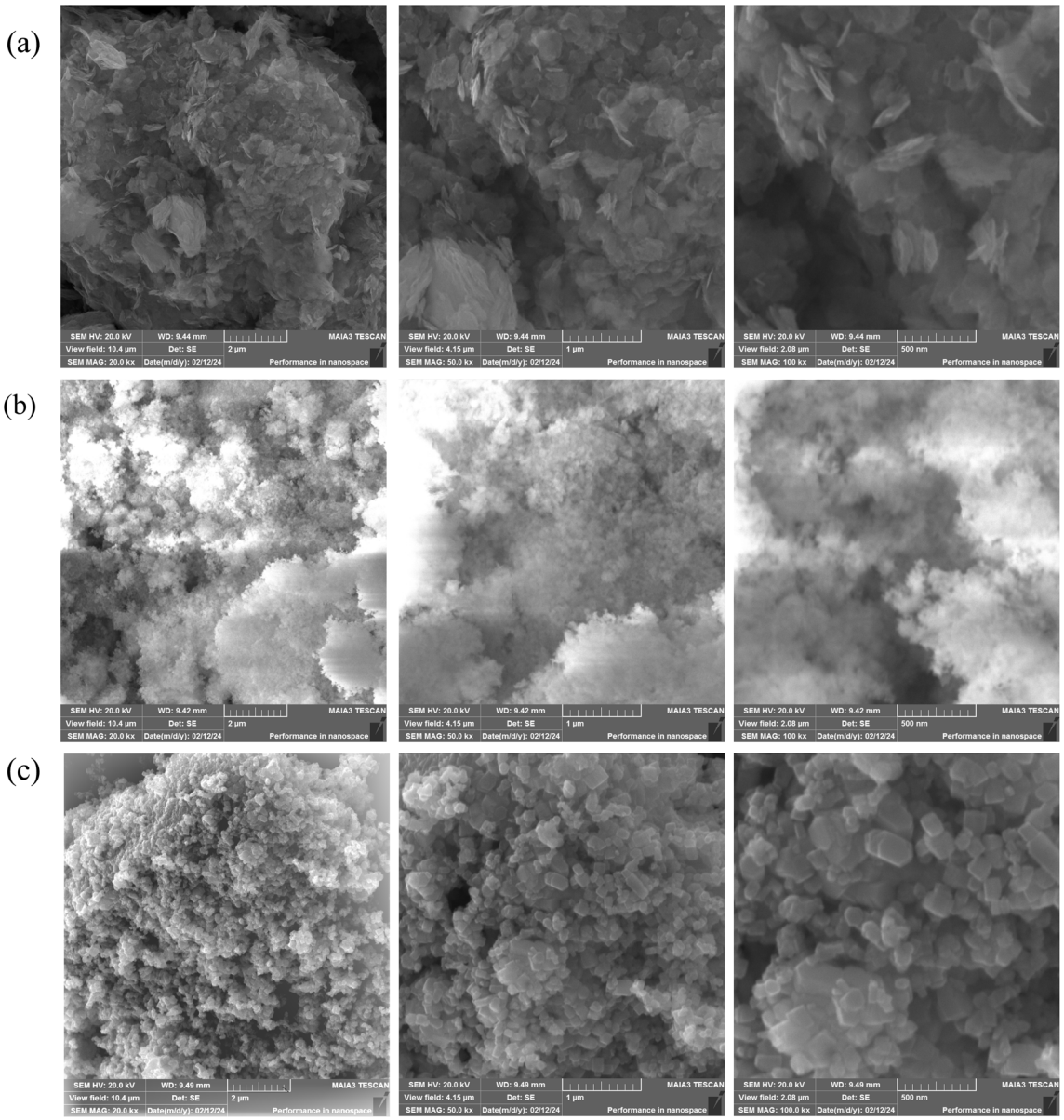


Fig. 5 SEM images at different resolutions (2 μm, 1 μm, and 500 nm) of (a) $Co_3O_4$, (b) CuO, and (c) ZnO nanoparticles.

surfaces with a cloud-like appearance. The SEM image of the ZnO nanoparticles revealed a well-defined crystalline structure. At higher resolution, the nanoparticles were shown to be present as cylindrical crystals. The particle size distributions of the $Co_3O_4$, CuO, and ZnO nanoparticles were determined from the SEM micrographs using ImageJ software, and the measured diameters were analyzed by constructing histograms followed by Gaussian fitting, as shown in Fig. 6. More than 150 particles were measured to ensure statistical accuracy. All samples exhibit unimodal and near-symmetric distributions, indicating predominantly normal particle-size behavior with minimal agglomeration. The larger particle size observed in Fig. 5(b) compared to 5(a) and 5(c) is due to a higher degree of agglomeration, which can increase the apparent particle size. The mean particle sizes were 146.49 ± 45.15 nm for $Co_3O_4$, 176.37 ± 50.47 nm for CuO, and 123.61 ± 27.26 nm for ZnO. The ZnO nanoparticles show the narrowest distribution, reflecting better size uniformity, whereas $Co_3O_4$ and CuO display broader distributions, suggesting higher size dispersion arising from differences in nucleation, growth, and agglomeration. The observed size difference remains consistent with the morphological trends.

### 3.5. XRD analysis of nanoparticles

The crystalline phases of the synthesized metal oxide nanoparticles, including $Co_3O_4$, CuO, and ZnO were confirmed by XRD analysis. Table 3 summarizes the crystallite size and SSA calculated using the above-mentioned method. A significant difference was observed between the particle size obtained from SEM and the crystallite size calculated from XRD. This is

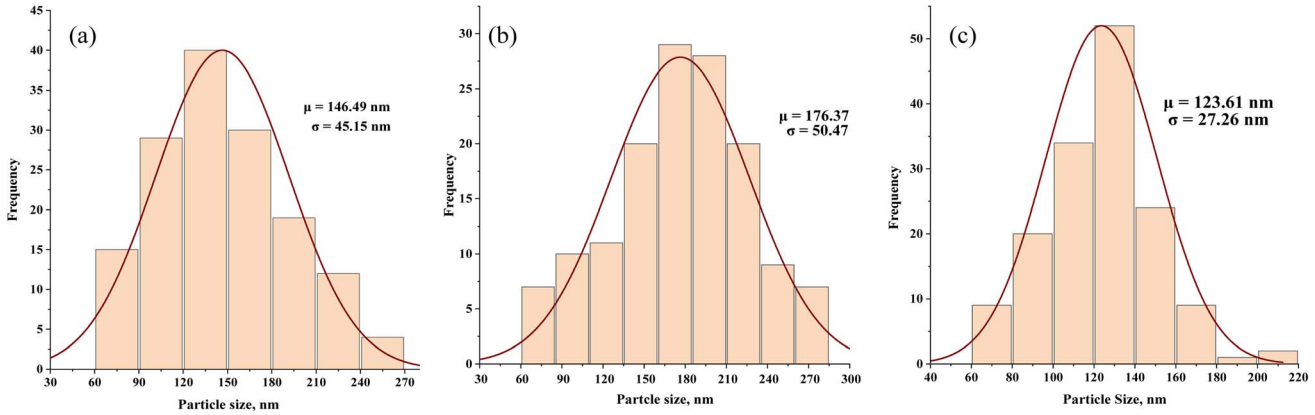


Fig. 6 Particle size distribution histograms with Gaussian fitting of (a) $Co_3O_4$, (b) CuO, and (c) ZnO nanoparticles.

because SEM measures aggregated or secondary particles, whereas XRD determines the size of individual crystallites. Nanoparticles tend to agglomerate, leading to a larger apparent particle size.[58] The XRD patterns of the synthesized nanoparticles are shown in Fig. 7.

The XRD pattern of the $Co_3O_4$ nanoparticles showed prominent peaks at 2$\theta$ values of 38.5°, 44.8°, 55.7°, and 65.2°, which correspond to the (222), (400), (422), and (440) planes, respectively.[59] The peaks align with the cubic spinel structure of $Co_3O_4$, as confirmed by the standard JCPDS card no. 00-42-1467 (Fig. S7). The mean crystallite size of $Co_3O_4$ nanoparticles was determined to be approximately 12.38 nm based on calculations using the Debye–Scherrer equation, as shown in Table S4.

The XRD pattern of the CuO nanoparticles displayed clear peaks at 2$\theta$ values that matched the monoclinic CuO crystal planes. The main peaks at 32.5°, 35.5°, 38.7°, 46.2°, 48.7°, 61.5°, 66.2°, and 68.1° correspond to the (110), (−111), (111), (−112), (−202), (−113), (−311), and (220) planes, respectively.[60] These peaks validated the production of monoclinic CuO and are consistent with the standard JCPDS card no. 01-089-5898, as shown in Fig. S8. The average crystallite size of CuO nanoparticles was calculated to be about 10.46 nm, calculated using the Debye–Scherrer formula, given in Table S5. Characteristic peaks with 2$\theta$ values of 31.7°, 34.4°, 36.2°, 47.5°, 56.6°, 62.8°, and 67.9° were seen in the X-ray diffraction spectra of ZnO nanoparticles; these peaks corresponded to the (100), (002), (101), (102), (110), (103), and (112) planes, respectively.[61] These identified peaks correspond to the hexagonal structure of ZnO, as shown by JCPDS card No. 00-036-1451, as given in Fig. S9. The crystallite size of the ZnO nanoparticles was determined to be around 11.76 nm, calculated using the Debye–Scherrer equation, as given in Table S6.

Table 3 Crystallite size and specific surface area of $Co_3O_4$, CuO, and ZnO

| S. No. | Metal oxide nanoparticles | Crystallite size (nm) | Specific surface area ($m^2\ g^{-1}$) |
|---|---|---|---|
| 1 | $Co_3O_4$ | 12.38 | 79.84 |
| 2 | CuO | 10.46 | 90.90 |
| 3 | ZnO | 11.76 | 90.94 |

### 3.6. Antibacterial activity of nanoparticles

Antibacterial assays were performed to determine the potential of the synthesized nanoparticles. For the determination of antibacterial activity, two strains of Gram-positive bacteria and two strains of Gram-negative bacteria were used. *Bacillus subtilis* and *Staphylococcus aureus* (Gram +ve) and *Escherichia coli* and *Pseudomonas aeruginosa* (Gram −ve) strains were used to assess the antibacterial potential of the samples. The drug levofloxacin was employed as a standard positive group. DMSO served as a negative control as it lacks activity against bacteria. Comparisons of the antibacterial assays are given in Table S7 and Fig. 8. The levofloxacin exhibited an inhibition zone of 32, 26, 29, and 27 mm against *B. subtilis*, *S. aureus*, *E. coli*, and *P. aeruginosa*, respectively, when 7 μL (7 mg/10 mL of DMSO) of the solution was used. The maximum activity was against the Gram-positive bacteria, while the potential of nanoparticles against the Gram-negative bacteria was low.

ZnO gave the maximum zone of inhibition (ZOI) against *Escherichia coli*, *Pseudomonas aeruginosa*, and *Bacillus subtilis* of 14, 14, and 15 mm, respectively, while against *Staphylococcus aureus*, CuO nanoparticles gave a maximum zone of inhibition of 15 mm; $Co_3O_4$ nanoparticles were not active against *Staphylococcus aureus.* Earlier studies have also demonstrated higher sensitivity of Gram-positive bacteria due to the absence of an outer lipopolysaccharide membrane, which facilitates nanoparticle penetration and interaction with the bacterial cell wall.[62–65] The antibacterial activity of the CL seed extract was evaluated as a control; however, no inhibition was observed against these strains, indicating that the antibacterial activity is primarily due to the incorporation and reduction of metal ions into nanoparticles, while the plant extract mainly facilitated the reduction and stabilization process.

### 3.7. Antioxidant activity of nanoparticles

The synthesized nanoparticles were evaluated based on their antioxidant activity. Three different methods were used: total phenolic content, DPPH assay, and ferric reduction potential.

**3.7.1. Total phenolic content.** Antioxidant activity was evaluated by determining the total phenolic content using the FC reagent. When phenolic compounds are present, they have

 

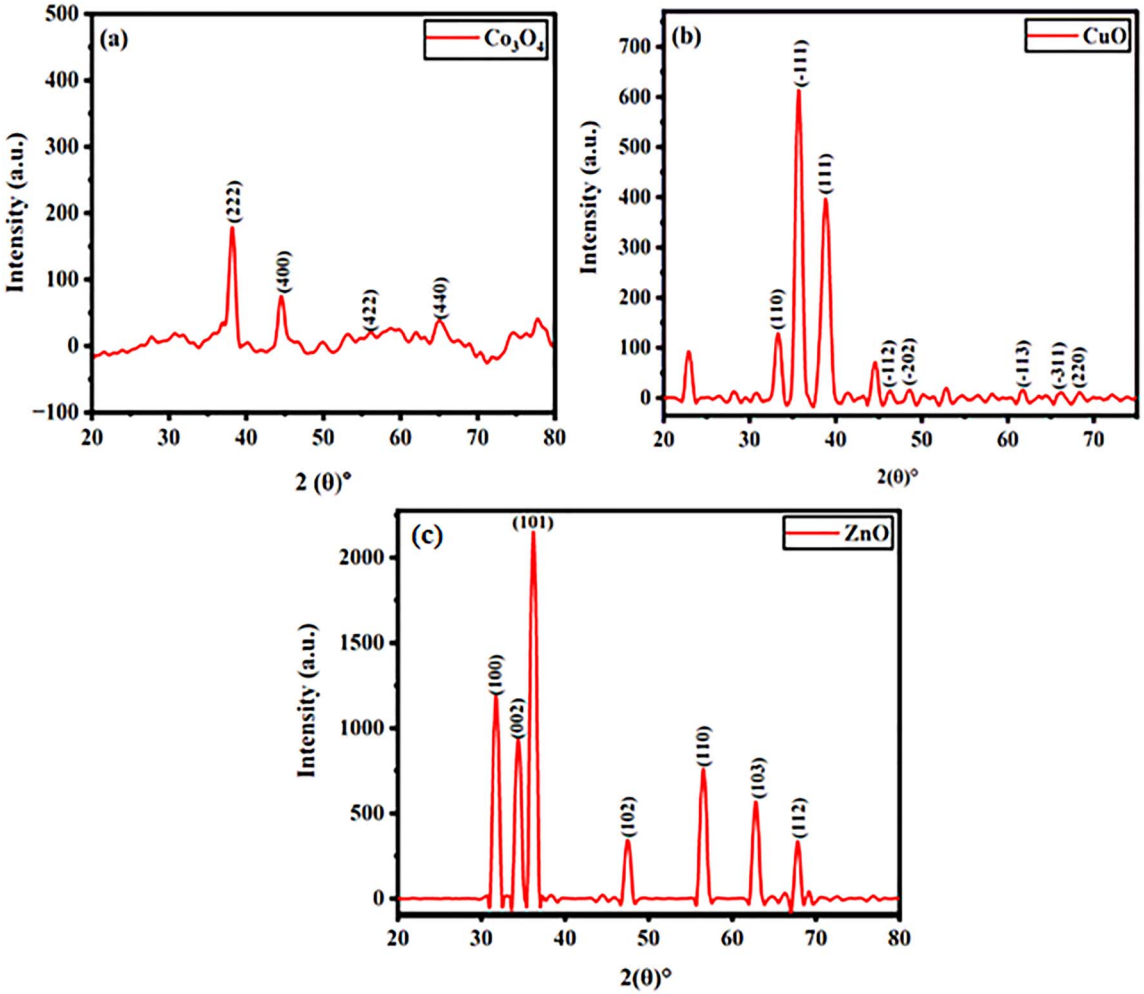


Fig. 7 XRD patterns of (a) $Co_3O_4$, (b) CuO, and (c) ZnO nanoparticles.

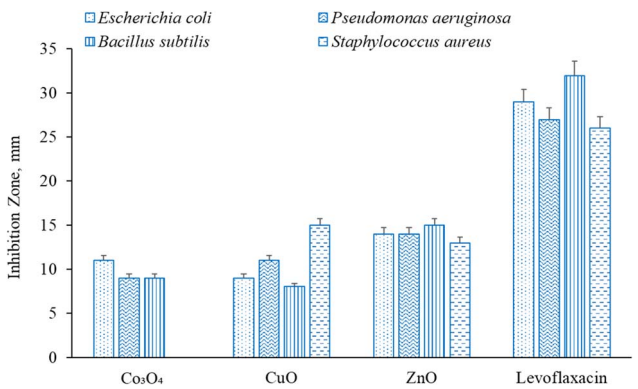


Fig. 8 Comparison of antibacterial activity of the synthesized nanoparticles.

a direct relationship with the antioxidant activity. The hydroxyl group present in the compounds has the potential for radical scavenging or can facilitate it through redox properties. The seed extracts contain phenolic compounds, including flavonoids, flavones, flavanols, cinnamic acid, protocatechuic acid, myricetin, *p*-coumaric acid, folic acid, and niacin. These compounds exhibit good antioxidant activity.[66] These compounds are responsible for the capping and stabilizing of the nanoparticles; they are entrapped within them and impart their properties. The Folin–Ciocalteu reagent was used to quantify the antioxidant activity, and the results are expressed as gallic acid equivalents. Gallic acid was used as a standard, as a naturally occurring phenol. An alkaline medium was required for the reaction to occur. The FC reagent, upon reduction, forms a blue complex that absorbs at 760 nm.[67] The total phenolic content of the CL seeds extract was found to be moderate, about 49%; however, a further increase was observed upon metal incorporation in the form of nanoparticles, which represented increased antioxidant potential. The best potential was given by ZnO nanoparticles, followed by CuO and $Co_3O_4$ nanoparticles with 81.81%, 49.24%, and 44.69%, respectively. The TPC values recorded are higher than those observed in literature for ZnO nanoparticles.[68]

**3.7.2. DPPH radical-scavenging activity.** The DPPH assay is the most common colorimetric assay used to determine the antioxidant activity of compounds. The nanoparticles were subjected to a DPPH assay to determine their radical-

scavenging activity by recording the absorbance at 517 nm. Butahydroxytoluene (BHT) was the standard used to evaluate and compare the activity of the nanoparticles. The CL seed extract exhibited a relatively low DPPH radical-scavenging activity of approximately 28%, indicating limited free radical reduction potential. The synthesized ZnO gave the best DPPH scavenging activity, with 90%, followed by cobalt oxide and copper oxide nanoparticles with 71% and 18%, respectively. The value for the DPPH assay of ZnO is higher than the previously reported literature values, whereas the CuO and $Co_3O_4$ activities were comparable to the previous results[69,70]

**3.7.3. Ferric reduction antioxidant potential.** FRAP assays of the samples were performed, with BHT as the standard. The CL seeds extract showed 23% activity, suggesting low electron-donating capacity. The cobalt oxide nanoparticles gave the maximum iron reduction potential, followed by zinc oxide nanoparticles and copper oxide nanoparticles, with percentage activity of 40.67, 36.72, and 25.4%, respectively. The results recorded for cobalt oxide were in the range of concentration dependence studies reported in the literature.[71] The synthesized nanoparticles were compared based on their antioxidant ability, and the results are listed in Table S8 and Fig. 9.

A comparison of the antioxidant assays revealed differences in activity trends. The variation among DPPH, FRAP, and total phenolic content assays can be attributed to the difference in their mode of action. The DPPH assay is based on free radical scavenging activity through the shifting of an H atom, while FRAP determines the reducing power of the nanoparticles *via* electron transfer. On the other hand, the concentration of phenolic compounds is determined by the total phenolic assay, reflecting the antioxidant activity. Furthermore, the enhanced performance of nanoparticles compared to the CL seed extract can be attributed to the incorporation of metallic ions, leading to increased surface area and enhanced interaction with reactive species, resulting in the higher antioxidant potential.

### 3.8. Enzyme inhibition activity of nanoparticles

Enzyme inhibition assays of the nanoparticles were conducted and evaluated against two enzymes: α-amylase and protease. The assays were conducted independently to assess the distinct biological functionalities of the nanoparticles. Protease inhibition serves as a representative model for evaluating interactions with serine proteases involved in various physiological and inflammatory processes. α-Amylase inhibition is widely employed to assess potential relevance in carbohydrate metabolism and glucose regulation.

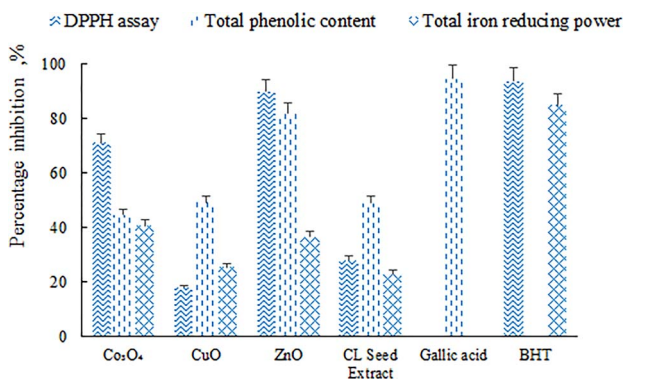


Fig. 9 Comparison of the antioxidant activities of the nanoparticles. Gallic acid and BHT are used as standard antioxidants. Values are expressed as mean ± SD ($n = 3$).

**3.8.1. Protease inhibition.** Protease enzymes break down proteins into their simple units. Trypsin is an enzyme that belongs to the class of proteases that digests proteins in the gut. The inhibition of trypsin was measured. The synthesized nanoparticles were used to study protease inhibition, and ZnO inhibited the protease enzyme by about 71%, followed by copper oxide nanoparticles, which inhibited the protease enzyme by 70%, and cobalt oxide nanoparticles inhibited the enzyme by 42%. In comparison, the standard protease inhibitor, aprotinin, demonstrated the highest inhibition (~78%), confirming the validity of the assay. Although limited studies are available specifically on trypsin inhibition by ZnO, CuO, and $Co_3O_4$ nanoparticles, previous reports on nanoparticle–enzyme interactions suggest that inhibition occurs through surface binding and structural modification of the enzymes. These findings are consistent with general reports of metal oxide nanoparticles exhibiting enzyme-inhibitory activity through physicochemical interactions with proteins.[72,73]

**3.8.2. α-Amylase inhibition.** The polysaccharides are converted into smaller units, *i.e.*, glucose and fructose, by α-amylase. In the blood, an excess of this enzyme causes hyperglycemia, a condition in which blood glucose levels increase. To keep the blood glucose at the required level, inhibitors are used.[74,75] DNSA reagents are used to perform the α-amylase inhibition assay. $Co_3O_4$ nanoparticles showed the highest inhibitory activity, about 62%, followed by ZnO (~48%) and CuO (~27%). The standard inhibitor, acarbose, exhibited strong α-amylase inhibition of ~73%, as a positive control. The recorded value of α-amylase inhibition is in the reported range of dose-dependent concentrations of ZnO and $Co_3O_4$ evaluated in the literature,[76,77] and higher than reported values for CuO.[78]

The CL seeds extract exhibited comparatively low inhibitory activity, showing 40% inhibition against protease and 35% inhibition against α-amylase. This indicates its limited enzyme inhibitory potential in the absence of metal incorporation. The comparison of nanoparticles based on their enzyme-inhibition potential is given in Table S9 and Fig. 10.

A comparative evaluation of the metal oxide nanoparticles synthesized in the present study reveals distinct differences in their biological performance, despite having comparable nanoscale crystallite sizes. The differences in biological activities among ZnO, CuO, and $Co_3O_4$ nanoparticles can be assigned to their different physicochemical behaviors and interaction mechanisms with biological systems. Among the three systems, ZnO nanoparticles exhibited the highest antioxidant and overall biological activity, followed by CuO, while $Co_3O_4$ demonstrated relatively moderate performance. The enhanced performance of ZnO nanoparticles may be attributed to their favorable surface properties and higher interaction efficiency with biological systems. Antibacterial activity is primarily promoted by reactive oxygen species (ROS) generation, metal ion release, and

membrane disruption, where ZnO induces strong oxidative stress through ROS formation, CuO exerts additional toxicity *via* $Cu^{2+}$ ion release, disrupting proteins and membrane structure, and $Co_3O_4$ shows comparatively moderate effects due to aggregation and reduced surface area.[79,80] Antioxidant activity is governed by surface redox behavior and electron-transfer capability, where ZnO exhibits enhanced radical scavenging due to phytochemical capping and surface reactivity, CuO shows moderate activity *via* $Cu^{2+}/Cu^{+}$ redox cycling, and $Co_3O_4$ displays lower efficiency because of reduced active surface sites.[81] The observed enzyme inhibition may be attributed to interactions between the nanoparticle surface and enzyme active sites, such as electrostatic binding, coordination with amino acid residues, and structural alteration of proteins, potentially leading to conformational changes and reduced catalytic activity. CuO often exhibits stronger inhibition due to metal ion interactions with thiol and imidazole groups, while ZnO also shows notable inhibition *via* surface adsorption, and $Co_3O_4$ demonstrates lower activity due to aggregation effects.[82] Overall, these variations confirm that the biological activity is governed by ROS generation, redox behavior, metal ion release, and surface functionalization rather than particle size alone.

In comparison to the previously reported green-synthesized nanoparticles, the present study shows that the difference in particle size and structure leads to differences in biological potential. Additionally, compared to chemically synthesized nanoparticles, this study reveals increased biocompatibility due to the presence of natural functional groups that act as reducing and stabilizing agents. In the literature, $Co_3O_4$ nanoparticles exhibit size- and surface-dependent biological properties, with significant variations reported depending on the synthesis approach. For instance, *Nodosilinea nodulosa* extract served as a reducing agent to synthesize $Co_3O_4$-NPs with a crystallite size of about 41 nm and a spherical shape. At 200 μg $mL^{-1}$, it exhibited 58.1% activity in the DPPH assay and 7.31 mm ZOI against *Bacillus safensis*.[83] Moreover, *Mollugo oppositifolia* L. leaf extract was used to synthesize $Co_3O_4$, with a crystallite size of around 22.7 nm and a spherical morphology of the nanoparticles, which were effective against *C. albicans* (MIC of 1 μg $mL^{-1}$).[84] In contrast, when the cobalt oxide nanoparticles were synthesized using the thermal-decomposition method, SEM analysis revealed an irregular shape with an average particle size of 44.66 nm and higher radical scavenging activity (about 81%); in addition, antibacterial activity was recorded against *E. coli* and *S. aureus* with ZOIs of 29 and 18 mm, respectively.[85] In the present study, where cobalt oxide nanoparticles were formed as agglomerated flakes with a crystallite size of 12.38 nm, the nanoparticles show moderate antibacterial activity against *E. coli*, with a ZOI of 12 mm, and were not active against *S. aureus.* They also demonstrated antioxidant potential with about 71% activity in the DPPH assay. The observed variation in biological performance, despite the smaller crystallite size, may be attributed to particle agglomeration and morphology, which can reduce the effective surface area available for interaction with microbial cells. Furthermore, differences in surface functionalization and phytochemical capping may also influence the overall biological efficacy.

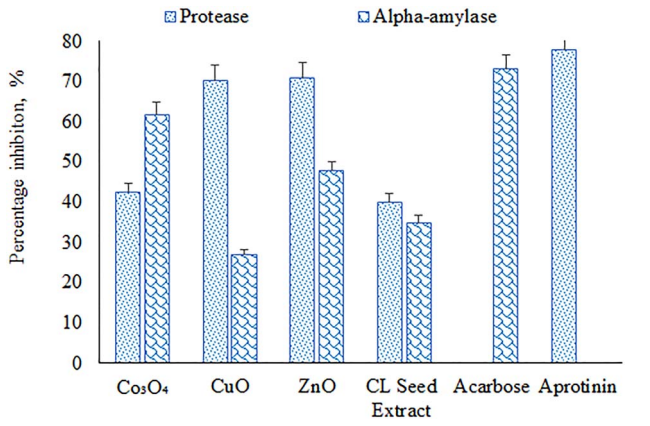


Fig. 10 Protease and α-amylase inhibition activities of $Co_3O_4$, CuO, and ZnO nanoparticles. Aprotinin and acarbose were used as standard inhibitors for protease and α-amylase, respectively. Values are expressed as mean ± SD ($n = 3$).

Similarly, CuO nanoparticles synthesized *via* green and chemical methods show significant differences in their structural and biological properties. In the literature, CuO synthesized from the leaf extract of *Morinda citrifolia* demonstrated spherical morphology with a size range of 20–50 nm. These nanoparticles exhibited 13.6 ± 1.1 mm ZOI against *Bacillus subtilis*.[86] In another study, CuO nanoparticles synthesized utilizing *Cocculus hirsutus* leaf extract exhibited a sheet-like structure with a size of 64.46 nm, and a ZOI of 27.86 mm was observed against *B. subtilis*. The maximum α-amylase activity was reported to be about 64.5%.[87] Furthermore, *Ixiolirion tataricum* was employed to synthesize CuO nanoparticles that exhibited a monoclinic structure with a size of 6.0 nm. Tyrosinase and α-amylase inhibition were reported to be 57.35 KAE $g^{-1}$ and 1.19 ACAE $g^{-1}$, respectively. DDPH and FRAP assays showed activities of 21.52 and 43.45 mg TE $g^{-1}$, respectively. However, despite their smaller size, these nanoparticles exhibited very low antibacterial activity (ZOI ≈ 4 mm), indicating that particle size alone does not govern biological performance.[88] In contrast, CuO synthesized *via* the chemical route demonstrated a needle-like morphology with a crystallite size of 25 nm. The maximum antibacterial potential was against *C. albicans* (ZOI = 17 mm). The DPPH assay showed 41.28% radical scavenging potential at 100 μg $mL^{-1}$.[89]

Beyond the biological applications, the use of CuO nanoparticles to reverse environmental damage has also been explored. For instance, a CuO–kaolin nanocomposite synthesized *via* a green route using *Citrullus lanatus* rind exhibited a high specific surface area (174.2 $m^2$ $g^{-1}$) and allowed effective regulation of aquaculture effluent parameters, including pH, chemical oxygen demand (COD), and removal/uptake of heavy metals. In contrast to the present study, which focuses on biological activities such as antibacterial, antioxidant, and enzyme inhibition, the performance in that system is primarily attributed to increased SSA and adsorption capacity provided by the composite matrix. This illustrates that the functional application of CuO-based materials is highly dependent on structural design.[35] Compared to these studies, the CuO nanoparticles

synthesized in the present work exhibit a crystallite size of 10.46 nm and a monoclinic crystal structure. The nanoparticles demonstrate notable antibacterial inhibition against *S. aureus* (ZOI = 15 mm). In addition, the synthesized CuO nanoparticles exhibit appreciable antioxidant and enzyme inhibitory potential, with approximately 45% total phenolic content and 70% protease inhibition.

The literature on ZnONPs based on *Citrullus lanatus* reports a particle size range of 10–50 nm, which is smaller than that observed in the present study. The antioxidant performance is largely comparable, particularly for DPPH radical scavenging (~90%), while the reported reducing power activity (80.54%) is notably higher than that obtained in the current work (36.72%), suggesting variations in surface chemistry and phytochemical capping. Enzyme inhibition studies in the literature also demonstrate significant activity, including 75.24% proteinase inhibition along with strong, concentration-dependent inhibition of α-amylase, β-glucosidase, and DPP-IV, whereas the present study exhibits comparatively moderate α-amylase and protease inhibition. Both studies consistently report broad-spectrum antibacterial activity against *Escherichia coli* and *Pseudomonas aeruginosa*, indicating the stable antimicrobial potential of ZnONPs synthesized using *Citrullus lanatus*. Overall, despite differences in particle size and certain bioactivity levels, both systems exhibit comparable biological performance, confirming the effectiveness of *Citrullus lanatus* phytochemicals in mediating the synthesis and functional properties of ZnO nanoparticles.[34] In the literature, ZnO was synthesized using the flower extract of *Nyctanthes arbor-tristis* (Nat). The crystallite size obtained was 15.8 nm. SEM images revealed the triangular shape of the nanoparticles, with an average size of 115.40 nm. They were biocompatible and hemocompatible and exhibited potent anticancer activity against cervical and lung cells.[90] Moreover, ZnO nanoparticles synthesized utilizing *Euterpe oleracea* Mart. Demonstrated an average particle size of 60 nm, with spherical morphology, and exhibited an antioxidant activity of 140.78 μmol $g^{-1}$. These nanoparticles gave a maximum zone of inhibition of 11.25 mm against *S. aureus*.[91] ZnO fabricated using the leaves of *J. schimperiana* with a crystallite size of 15.27 nm gave a maximum zone of inhibition of 21.42 mm against *S. epidermidis*.[92] ZnO prepared using a solvothermal method exhibited a crystallite size of 12.6 nm. High agglomeration was observed in the SEM images, which may have affected its antibacterial activity. The zone of inhibition was recorded as 10 mm at a concentration of 2 mg $mL^{-1}$ against *B. subtilis*.[93] This suggests that a lack of natural capping agents may lead to particle agglomeration, reducing the effective surface area for biological interactions. Compared to these studies, the ZnO nanoparticles synthesized in the present work exhibit a smaller crystallite size of 11.76 nm. SEM images revealed a hexagonal structure, and a higher biological activity was observed, including a ZOI of 15 mm against *S. aureus*, along with significant antioxidant activity (90% DPPH scavenging and 81% total phenolic content) and notable protease inhibition. These findings indicate that, beyond particle size alone, the surface chemistry and biofunctionalization imparted by plant-derived compounds play a crucial role in determining the overall biological efficacy of ZnO nanoparticles.

This variation can be attributed to differences in the phytochemical composition of the plant extracts used during green synthesis, which significantly influence nanoparticle nucleation, growth, and surface functionalization. Unlike many reported systems, where aggregation or limited capping reduces biological efficiency, the nanoparticles in the present study likely benefit from more effective stabilization and surface biofunctionalization, leading to enhanced interaction with microbial cells and enzymes. The results highlight that, beyond particle size, factors such as morphology, dispersion stability, and surface chemistry play a decisive role in determining the biological potential of $Co_3O_4$, CuO and ZnO nanoparticles.

# 4. Conclusion

In this research work, seed extract of *Citrullus lanatus* was utilized as a natural photochemical medium to facilitate the reduction, stabilization and capping process for the green synthesis of cobalt, copper, and zinc oxide nanoparticles. The synthesized nanoparticles were effectively characterized using UV-vis, FT-IR spectroscopy, XRD, SEM, and EDX techniques. Optical studies confirmed the nucleation and growth of metal oxide nanoparticles with characteristic absorption bands and tunable band-gap energies. FT-IR analysis revealed the participation of bio-active phytochemicals in the capping and stabilization of fabricated nanoparticles, whereas XRD confirmed their crystalline nature with nanoscale crystallite sizes. SEM analysis demonstrated particles with sizes spanning 120–170 nm with distinct surface morphology, whereas EDX verified the elemental purity of the synthesized oxides. The nanoparticles also exhibited high specific surface areas, highlighting their potential suitability for various functional applications.

Biological evaluation demonstrated significant antibacterial, antioxidant, and enzyme inhibitory activities, with ZnO exhibiting the highest overall antibacterial and antioxidant performance, while CuO and $Co_3O_4$ showed selective activity against specific bacterial strains and enzymes. The variation in biological responses among the nanoparticles can be attributed to differences in metal oxide composition, crystallite size, surface area, and surface chemistry arising from metal-specific interactions with the seed extract.

The green-synthesized $Co_3O_4$, CuO, and ZnO nanoparticles exhibit strong potential for future applications in biomedical, environmental, food packaging, and catalytic fields. Their multifunctional biological activity, combined with sustainable synthesis, highlights their suitability for next-generation eco-friendly nanomaterials.

Despite the promising results, this study is limited by the absence of mechanical insights, toxicity evaluation, and advanced characterization techniques such as BET and TEM analyses. Future work should focus on controlling agglomeration, elucidating structure–activity relationships, evaluating cytotoxicity and biocompatibility, and exploring practical biomedical and environmental applications of these green-synthesized nanoparticles.

## Author contributions

Wajeeha Gohar: writing – original draft, investigation, methodology; Khalil Nawaz: formal analysis; Wardha Zafar: writing – review & editing, visualization; Ambreen Nasir Cheema: data curation; Nadeem Raza: validation; Muddassar Zafar: formal analysis; Muhammad Faizan Nazar: formal analysis; and Sajjad Hussain Sumrra: supervision, project administration, conceptualization.

## Conflicts of interest

The authors declare that they have no known competing financial interests or personal relationships that could have appeared to influence the work reported in this paper.

## Data availability

The data that support the findings of this study are available from the corresponding author on request.

Supplementary information (SI) is available. See DOI: https://doi.org/10.1039/d6ra02015a.

## References

1 L. Abdulazeem, F. G. Hassan, M. J. Abed, W. S. Torki and A. S. Naje, *Glob. Nest J.*, 2022, **25**, 1–5.
2 S. A. M. Ealia and M. P. Saravanakumar, *IOP Conf. Ser.: Mater. Sci. Eng.*, 2017, **263**, 032019.
3 A. S. Dousari, S. S. Hosseininasab, M. R. Akbarizadeh, M. Naderifar and N. Satarzadeh, *Sci. Hortic.*, 2023, **320**, 112215.
4 S. Ying, Z. Guan, P. C. Ofoegbu, P. Clubb, C. Rico, F. He and J. Hong, *Environ. Technol. Innov.*, 2022, **26**, 102336.
5 M. Thatyana, N. P. Dube, D. Kemboi, A. L. E. Manicum, N. S. Mokgalaka-Fleischmann and J. V. Tembu, *Nanomaterials*, 2023, **13**, 2616.
6 H. Singh, M. F. Desimone, S. Pandya, S. Jasani, N. George, M. Adnan and S. A. Alderhami, *Int. J. Nanomed.*, 2023, **18**, 4727–4750.
7 L. Chen, X. Zhou and C. He, *Wiley Interdiscip. Rev. Nanomed. Nanobiotechnol.*, 2019, **11**, e1573.
8 Y. Dang and J. Guan, *Smart Mater. Med.*, 2020, **1**, 10–19.
9 F. Herranz, E. Almarza, I. Rodríguez, B. Salinas, Y. Rosell, M. Desco and J. Ruiz-Cabello, *Microsc. Res. Tech.*, 2011, **74**, 577–591.
10 H. L. Loo, B. H. Goh, L. H. Lee and L. H. Chuah, *Asian J. Pharm. Sci.*, 2022, **17**, 299–332.
11 S. Logambal, C. Maheswari, S. Chandrasekar, T. Thilagavathi, C. Inmozhi, S. Panimalar and K. Kanimozhi, *J. King Saud Univ. Sci.*, 2022, **34**, 101910.
12 I. S. Tania, M. Ali and M. Akter, *J. Eng. Fibers Fabr.*, 2022, **17**, 15589250221136378.
13 S. Zhang, W. Zhao, J. Zeng, Z. He, X. Wang, Z. Zhu and Q. Wang, *Mater. Today Bio*, 2023, **20**, 100638.
14 A. Ibrahim, M. R. Ramadan, A. E. M. Khallaf and M. Abdulhamid, *Environ. Sci. Pollut. Res.*, 2023, **30**, 106838–106859.
15 T. Nshizirungu, M. Rana, M. I. H. Khan, Y. T. Jo and J. H. Park, *J. Hazard. Mater. Adv.*, 2023, **9**, 100242.
16 R. S. Dangana, R. C. George and F. K. Agboola, *Green Chem. Lett. Rev.*, 2023, **16**, 2169591.
17 M. Ansari, S. Ahmed, M. T. Khan, N. A. Hamad, H. M. Ali, A. Abbasi and I. K. Jasim, *Horticulturae*, 2023, **9**, 369.
18 F. Dehghani, S. Mosleh-Shirazi, M. Shafiee, S. R. Kasaee and A. M. Amani, *Appl. Nanosci.*, 2023, **13**, 4395–4405.
19 P. Suresh, A. Doss, R. P. Praveen Pole and M. Devika, *Biomass Convers. Biorefin.*, 2024, **14**, 16451–16459.
20 D. H. Atha, H. Wang, E. J. Petersen, D. Cleveland, R. D. Holbrook, P. Jaruga and B. C. Nelson, *Environ. Sci. Technol.*, 2012, **46**, 1819–1827.
21 R. Chauhan, A. Kumar, R. Tripathi and A. Kumar, Advancing of zinc oxide nanoparticles for cosmetic applications, in *Handbook of Consumer Nanoproducts*, ed. V. R. Preedy and V. B. Patel, Springer, Singapore, 2022, pp. 1–16.
22 L. Cai, C. Liu, G. Fan, C. Liu and X. Sun, *Environ. Sci.: Nano*, 2019, **6**, 3653–3669.
23 V. D. Rajeswari, A. S. Khalifa, A. Elfasakhany, I. A. Badruddin, S. Kamangar and K. Brindhadevi, *Appl. Nanosci.*, 2023, **13**, 1367–1375.
24 L. Chompunut, T. Wanaporn, W. Anupong, M. Narayanan, M. Alshiekheid, A. Sabour and R. Shanmuganathan, *Food Chem. Toxicol.*, 2022, **166**, 113245.
25 B. Naiel, M. Fawzy, M. W. A. Halmy and A. E. D. Mahmoud, *Sci. Rep.*, 2022, **12**, 20370.
26 A. Ekennia, D. Uduagwu, O. Olowu, O. Nwanji, O. Oje, B. Daniel and C. Emma-Uba, *Micron*, 2021, **141**, 102964.
27 M. Kumar, D. Kaushik, A. Kumar, P. Gupta, C. Proestos, E. Oz, E. Orhan, J. Kaur, M. R. Khan, T. Elobeid and M. Bordiga, *Int. J. Food Sci. Technol.*, 2023, **58**, 2883–2892.
28 S. Kota, P. Dumpala, R. Sajja and R. Anantha, *Sci. Rep.*, 2024, **14**, 30857.
29 G. F. Alka, A. S. Anamika and P. Ranu, *J. Pharmacogn. Phytochem.*, 2018, **7**, 2222–2225.
30 A. Singh and V. Kumar, *Food Front*, 2022, **3**, 182–193.
31 S. H. Gebre, *J. Cluster Sci.*, 2023, **34**, 665–704.
32 D. K. Bhui, H. Bar, P. Sarkar, G. P. Sahoo, S. P. De and A. Misra, *J. Mol. Liq.*, 2009, **145**, 33–37.
33 R. Das and S. Sarkar, *Indian J. Pure Appl. Phys.*, 2018, **56**, 765–772.
34 R. Ishwarya, J. Jeyavani, J. Jayakumar, S. Alarifi, M. Govindarajan, M. Nicoletti and B. Vaseeharan, *J. Indian Chem. Soc.*, 2022, **99**, 100703.
35 A. M. Aibinu, T. A. Folorunso, A. A. Saka, L. A. Ogunfowora, K. O. Iwuozor and J. O. Ighalo, *Reg. Stud. Mar. Sci.*, 2022, **52**, 102308.
36 G. F. Aaga and S. T. Anshebo, *Heliyon*, 2023, **9**, e16067.
37 B. Rahul, M. S. Roji, H. P. Kumar and V. Thiruchelvam, *AIP Conf. Proc.*, 2024, **3161**, 020233.
38 A. N. Cheema, I. Muneer, F. Yasmeen and D. Ali, *Mater. Sci. Eng. B*, 2025, **312**, 117878.
39 D. L. Crittenden, *AIP Adv.*, 2023, **13**, 115323.

40 A. M. Amini and S. Shahroodian, *Inorg. Nano-Metal Chem.*, 2025, **55**, 520–526.
41 C. Singh, S. K. Anand, R. Upadhyay, N. Pandey, P. Kumar, D. Singh and R. Tilak, *Mater. Chem. Phys.*, 2023, **297**, 127413.
42 A. Blainski, G. C. Lopes and J. C. P. De Mello, *Molecules*, 2013, **18**, 6852–6865.
43 T. Hasara, M. A. Salam and M. Kandiah, *BMS J. Appl. Learn.*, 2023, **1**, 73–83.
44 E. M. Njoya, in *Cancer*, eds V. R. Preedy and V. B. Patel, Academic Press, San Diego, CA, 2021, pp. 349–357.
45 S. Baliyan, R. Mukherjee, A. Priyadarshini, A. Vibhuti, A. Gupta, R. P. Pandey and C. M. Chang, *Molecules*, 2022, **27**, 1326.
46 A. Lalitha, R. Subbaiya and P. Ponmurugan, *Int. J. Curr. Microbiol. Appl. Sci.*, 2013, **2**, 228–235.
47 I. F. Benzie and J. J. Strain, *Anal. Biochem.*, 1996, **239**, 70–76.
48 N. Kanmaz, A. Uzer, J. Hizal and R. Apak, *Talanta*, 2020, **216**, 120960.
49 G. G. Guzmán, B. A. A. Garza, R. C. Ríos, N. W. Minsky and R. S. Aranda, *Quim. Nova*, 2022, **45**, 1146–1152.
50 M. N. Wickramaratne, J. C. Punchihewa and D. B. M. Wickramaratne, *BMC Complement. Altern. Med.*, 2016, **16**, 1–5.
51 U. Patil, K. A. Baloch, S. H. Nile, J. T. Kim and S. Benjakul, *Foods*, 2023, **12**, 2937.
52 M. Mittal, M. Sharma and O. P. Pandey, *Sol. Energy*, 2014, **110**, 386–397.
53 M. M. Eid, Characterization of nanoparticles by FTIR and FTIR-microscopy, in *Handbook of Consumer Nanoproducts*, eds V. R. Preedy and V. B. Patel, Springer, Singapore, 2022, pp. 1–30.
54 S. P. Wallbridge, K. Lawson, A. E. Catling, C. A. Kirk and S. E. Dann, *Dalton Trans.*, 2022, **51**, 18010–18023.
55 D. M. Mamand, S. A. Hussen and S. B. Aziz, *Sci. Rep.*, 2025, **15**, 3130.
56 A. Fatoni, A. C. Paramita, B. Untari and N. Hidayati, *J. Kim. Sains Apl.*, 2020, **23**, 432–439.
57 Y. Xu, P. Liu and Y. Zhang, *Spectrochim. Acta A*, 2022, **264**, 120256.
58 B. Ebin, E. Arıg, B. Özkal and S. Gürmen, *Int. J. Miner. Metall. Mater.*, 2012, **19**, 651–656.
59 J. Sun, H. Wang, Y. Li and M. Zhao, *J. Porous Mater.*, 2021, **28**, 889–894.
60 V. Anusha, A. Raju, B. R. Kumar, G. M. Rao, K. Samatha, N. K. Rotte and K. Kaviyarasu, *Appl. Phys. A*, 2026, **132**, 143.
61 C. R. Mendes, G. Dilarri, C. F. Forsan, V. D. M. R. Sapata, P. R. M. Lopes, P. B. de Moraes and E. D. Bidoia, *Sci. Rep.*, 2022, **12**, 2658.
62 A. Sirelkhatim, S. Mahmud, A. Seeni, N. H. M. Kaus, L. C. Ann, S. K. M. Bakhori and D. Mohamad, *Nano-Micro Lett.*, 2015, **7**, 219–242.
63 H. Upadhyaya, S. Shome, R. Sarma, S. Tewari, M. K. Bhattacharya and S. K. Panda, *Am. J. Plant Sci.*, 2018, **9**, 1279–1291.
64 A. Nieto-Maldonado, S. Bustos-Guadarrama, H. Espinoza-Gomez, L. Z. Flores-López, K. Ramirez-Acosta, G. Alonso-Nuñez and R. D. Cadena-Nava, *J. Environ. Chem. Eng.*, 2022, **10**, 107130.
65 A. A. Abass, W. K. Alaarage, N. H. Abdulrudha and J. Haider, *J. Med. Life*, 2021, **14**, 823.
66 A. Zeb, *J. Food Biochem.*, 2020, **44**, e13394.
67 S. Aryal, M. K. Baniya, K. Danekhu, P. Kunwar, R. Gurung and N. Koirala, *Plants*, 2019, **8**, 96.
68 B. H. Kiani, F. Ikram, H. Fatima, A. Alhodaib, I. U. Haq, T. Ur-Rehman and I. Naz, *Sci. Rep.*, 2022, **12**, 10024.
69 E. A. Shalaby, S. M. Shanab, W. M. A. El-Raheem and E. A. Hanafy, *Sci. Rep.*, 2022, **12**, 18400.
70 I. Ryntathiang, A. Behera, T. Richard and M. K. D. Jothinathan, *Cureus*, 2024, **16**, e59112.
71 P. D. Sarvalkar, A. S. Jamadar, A. B. Magdum, P. K. Pawar, J. B. Yadav, M. S. Nimbalkar and K. K. K. Sharma, *Results Eng.*, 2024, **22**, 102094.
72 B. Junejo, Q. A. Solangi, A. S. B. Thani, I. M. Palabiyik, T. Ghumro, N. Bano and S. I. H. Taqvi, *World J. Microbiol. Biotechnol.*, 2023, **39**, 220.
73 G. Murugappan and K. J. Sreeram, *Colloids Surf. B*, 2021, **197**, 111386.
74 P. M. Sales, P. M. Souza, L. A. Simeoni, P. O. Magalhães and D. Silveira, *J. Pharm. Pharm. Sci.*, 2012, **15**, 141–183.
75 L. Gong, D. Feng, T. Wang, Y. Ren, Y. Liu and J. Wang, *Food Sci. Nutr.*, 2020, **8**, 6320–6337.
76 K. Vijayalakshmi, N. Vidhyulatha, S. Aldawood, A. Manjulabai, M. Aboorva, R. Manjula and K. Nagaraj, *Food Biosci.*, 2025, **68**, 106371.
77 G. Vanitha, R. Manikandan, A. Prakasam, M. D. Navinkumar, K. Sathiyamoorthi and B. Dhinakaran, *J. Sci. Res.*, 2023, **15**, 667–684.
78 M. Asghar, A. Sajjad, S. Hanif, J. S. Ali, Z. Ali and M. Zia, *Mater. Chem. Phys.*, 2022, **278**, 125724.
79 Y. N. Slavin, J. Asnis, U. O. Häfeli and B. Bach, *J. Nanobiotechnol.*, 2017, **15**, 65.
80 A. K. Chatterjee, R. Chakraborty and T. Basu, *Nanotechnology*, 2014, **25**, 135101.
81 A. V. Samrot, S. P. R. Singh, R. Deenadhayalan, V. V. Rajesh, S. Padmanaban and K. K. Radhakrishnan, *Oxygen*, 2022, **2**, 591–604.
82 S. Sabella, R. P. Carney, V. Brunetti, M. A. Malvindi, N. Al-Juffali, G. Vecchio and P. P. Pompa, *Nanoscale*, 2014, **6**, 7052–7061.
83 F. Aslam, L. A. Minhas, M. Kaleem, A. Jabeen, A. Akram, H. A. Malik and A. S. Mumtaz, *BioNanoSci*, 2024, **14**, 4764–4778.
84 P. Gowthami, A. Kosiha, S. Meenakshi, G. Boopathy, A. G. Ramu and D. Choi, *Sci. Rep.*, 2023, **13**, 9002.
85 D. Das and B. J. Saikia, *Chem. Phys. Impact.*, 2023, **6**, 100137.
86 M. Priya, R. Venkatesan, S. Deepa, S. S. Sana, S. Arumugam, A. Karami and S. C. Kim, *Sci. Rep.*, 2023, **13**, 18838.
87 S. Ameena, N. Rajesh, S. M. Anjum, H. Khadri, K. Riazunnisa, A. Mohammed and Z. A. Kari, *Appl. Biochem. Biotechnol.*, 2022, **194**, 4424–4438.
88 H. I. M. Amin, A. H. Hamadamin, K. D. Issa, S. H. Shareef, V. S. Abdullah, H. O. Othman and G. Zengin, *Inorg. Chem. Commun.*, 2025, **184**, 116024.

89 V. Pradeep, P. Veerakumar and V. P. Veeraraghavan, *Cureus*, 2024, **16**, e51678.
90 S. C. Chabattula, P. K. Gupta, K. Govarthanan, S. Varadaraj, S. K. Rayala, D. Chakraborty and R. S. Verma, *Appl. Biochem. Biotechnol.*, 2024, **196**, 382–399.
91 I. R. S. Vieira, A. A. da Silva, B. D. da Silva, L. Torres Neto, L. Tessaro, A. K. O. Lima and C. A. Conte-Junior, *Waste Biomass Valoriz.*, 2024, **15**, 4717–4734.
92 D. E. Yizengaw, E. M. Godie and A. H. Manayia, *Inorg. Chem. Commun.*, 2025, **174**, 114071.
93 M. Iqbal, A. Ibrar, A. Ali, F. H. Memon, F. Rehman, Z. Bhatti and K. H. Thebo, *Int. Nano Lett.*, 2022, **12**, 205–213.